coatings

MDPI

Article

Combined Raman Spectroscopy and Magneto-Transport Measurements in Disordered Graphene: Correlating Raman D Band and Weak Localization Features

Isaac Childres [1,2,†], Yaping Qi [3,4,*,†], Mohammad A. Sadi [2,5], John F. Ribeiro [2,5], Helin Cao [1,2] and Yong P. Chen [1,2,3,4,5,6,*]

1 Department of Physics and Astronomy, Purdue University, West Lafayette, IN 47907, USA
2 Birck Nanotechnology Center, Purdue University, West Lafayette, IN 47907, USA
3 Macau Institute of Systems Engineering, Macau University of Science and Technology, Av. Wai Long, Macao SAR, China
4 Purdue Quantum Science and Engineering Institute, Purdue University, West Lafayette, IN 47907, USA
5 School of Electrical and Computer Engineering, Purdue University, West Lafayette, IN 47907, USA
6 Institute for Physics and Astronomy and Villum Centers for Dirac Materials and for Hybrid Quantum Materials and Devices, Aarhus University, 8000 Aarhus C, Denmark
* Correspondence: ypqi@must.edu.mo (Y.Q.); yongchen@purdue.edu (Y.P.C.); Tel.: +1-(765)-494-0947 (Y.P.C.)
† These authors contributed equally to this work.

Abstract: Although previous studies have reported the Raman and weak localization properties of graphene separately, very few studies have examined the correlation between the Raman and weak localization characterizations of graphene. Here, we report a Raman spectroscopy and low-magnetic-field electronic transport study of graphene devices with a controlled amount of defects introduced into the graphene by exposure to electron-beam irradiation and oxygen plasma etching. The relationship between the defect correlation length (L_D), calculated from the Raman "D" peak, and the characteristic scattering lengths, L_ϕ, L_i and L_*, computed from the weak localization effects measured in magneto-transport was investigated. Furthermore, the effect on the mean free path length due to the increasing amounts of irradiation incident on the graphene device was examined. Both parameters—including L_D and L_ϕ—decreased with the increase of irradiation, which was shown to be related to the increase of disorder through the concomitant decrease in the mean free path length, l. Although these are similar trends that have been observed separately in previous reports, this work revealed a novel nonlinear relationship between L_D and L_ϕ, particularly at lower levels of disorder. These findings are valuable for understanding the correlation between disorder in graphene and the phase coherence and scattering lengths of its charge carriers.

Keywords: Raman spectroscopy; weak localization; disorder; graphene

check for updates

Citation: Childres, I.; Qi, Y.; Sadi, M.A.; Ribeiro, J.F.; Cao, H.; Chen, Y.P. Combined Raman Spectroscopy and Magneto-Transport Measurements in Disordered Graphene: Correlating Raman D Band and Weak Localization Features. *Coatings* **2022**, *12*, 1137. https://doi.org/10.3390/coatings12081137

Academic Editor: Alicia de Andrés

Received: 21 May 2022
Accepted: 4 August 2022
Published: 7 August 2022

1. Introduction

Graphene has received much attention in the scientific community because of its distinct properties and potential in nanoelectronics applications [1,2]. Raman spectroscopy [3–5], which identifies vibrational modes using laser excitation, is a powerful, non-invasive method to measure many important characteristics of graphene [6], such as its layer number, defect density, and carrier concentration.

In pristine graphene, the Stokes phonon energy shift of laser excitation creates two main peaks in the Raman spectrum. The G peak (~1580 cm^{-1}) is the primary in-plane vibrational mode, and is caused by the E_{2g} phonon at the Γ point. Another major peak in graphene is 2D (~2700 cm^{-1}), which is believed to be created by a process of the double scattering of A_{1g} phonons between K and K′ with an electron–hole pair [4].

In disordered graphene, a third major Raman peak appears: the D peak (~1350 cm^{-1}). In order for the D peak to be present in the Raman spectrum, a charge carrier must be

excited and inelastically scattered by a phonon, and then elastically scattered by a lattice defect or grain boundary to recombine [7]. Disorder in graphene not only activates the D peak, which is caused by scattering from K to K′ (intervalley), but also gives rise to the D′ peak (~1620 cm^{-1}), which is formed by scattering from K to K (intravalley), and D + D′ (~2940 cm^{-1}), a combinational scattering peak [7]. As has been previously reported, due to the strong dependence of graphene's Raman D peak on disorder in graphene, the level of disorder in graphene can be characterized using the ratio of Raman peak intensities (I_D/I_G) [8–14]. As the disorder in graphene increases, I_D/I_G displays two different behaviors: a regime of "low defect density", where I_D/I_G will increase with the enhanced disorder because a higher defect density creates more elastic scattering, and a regime of "high defect density", where I_D/I_G will decrease with the increased disorder because a higher defect density results in a more amorphous carbon structure, attenuating all of the Raman peaks [7].

Disorder in graphene can also be characterized using electrical transport through the phenomenon of weak localization. Weak localization appears in disordered graphene samples as a peak in the resistivity, as a function of a magnetic field at zero magnetic field. At zero field, graphene's resistivity is increased by constructive interference between the time-reversed trajectories of phase-coherent carriers scattered off of defects [15]. A perpendicular magnetic field breaks the time-reversal symmetry, decreasing the resistivity as the field increases. The width of this weak localization feature is directly related to the phase coherence length, L_ϕ, the length through which coherent charge carriers travel before losing phase coherence. This low-field curve can be used to extract L_ϕ, as well as the intervalley and intravalley scattering lengths, L_i and L_*, respectively. Intravalley scattering is believed to be largely due to charge impurity disorder, while intervalley scattering is caused by sharp lattice defects.

Although previous reports have investigated these phenomena in disordered graphene separately [8–41], there are very few studies that examined the correlation between the Raman and weak localization characterizations of graphene [42–47]. Herein, the relationship between the Raman and weak localization properties of graphene as controlled amounts of disorder are introduced was investigated. This study provides important information for a better understanding of the relationship between defect correlation length (reflecting disorder density) in graphene and the phase coherence and scattering lengths of its charge carriers.

2. Materials and Methods

Our graphene samples were fabricated using a similar method to that described in our previous publications [13,14]. We performed the micromechanical exfoliation [2] of highly ordered pyrolytic graphite (HOPG, "ZYA" grade, from Momentive Performance Materials) onto a p-doped Si wafer with a 300 nm of overlayer SiO_2. Single-layer graphene flakes, typically of around 100 μm^2 in size, were identified using color contrast with an optical microscope [14,48] and then confirmed with Raman spectroscopy [7]. Graphene field-effect transistor (GFET) devices were then fabricated using electron-beam lithography (EBL). The electrical contacts (5 nm Cr/35 nm Au) were fabricated by electron-beam evaporation.

In order to study the effects of disorder, a GFET device was placed in the same scanning electron microscope (SEM) system used for EBL under high vacuum (10^{-6} torr) to undergo electron-beam irradiation [13], which is a common method to introduce defects in graphene [9,49,50]. An area of 25 μm by 25 μm including the graphene flake on the device was continuously scanned by the electron beam. The beam's kinetic energy was 30 keV, and the beam current was kept at 0.133 nA. The accumulated time exposed to the electron-beam (*Te*) determines the accumulated irradiation dosage (*Re*) (e.g., T_e = 75 s gives R_e = 100 e^-/nm^2). In comparison, the typical exposure used in our lithography process is around 1 e^-/nm^2. SEM imaging typically exposes samples to at least 100 e^-/nm^2.

After each successive exposure, the graphene device was removed from the SEM, and room-temperature Raman measurements were promptly performed using a 532-nm

excitation laser. The device was then placed in a probe station and cooled to 4 K at 10^{-6} mbar for the Hall electrical transport measurements.

In addition, we conducted measurements of graphene exposed to various amounts of oxygen plasma [14], as another method to create defects. Our graphene devices were exposed cumulatively to short pulses (~$\frac{1}{2}$ s) of oxygen plasma in a microwave plasma system (Plasma-Preen II-382) operating at 100 W. A constant flow of O_2 (3 sccm) was pumped through the sample space in a rough vacuum (540 Torr), and the gas was excited by microwaves (manually pulsed on and off), generating an ionized oxygen plasma, which has an etching effect on graphene and thus creates defects, which can be observed with AFM in high enough concentrations [14,51]. The microwave-excited plasma pulses were applied to the samples cumulatively, and field-effect and Raman measurements were performed as soon as possible (<5 min) in the ambient atmosphere and temperature after each pulse, in order to avoid any relaxation effects. The magneto-transport data were taken using a ^{3}He superconducting magnet probe several days after the plasma exposure.

From the Raman spectroscopy measurements, we extracted the defect correlation length, L_D, using

$$\frac{I_D}{I_G} = \frac{C'(\lambda)}{{L_D}^2} \tag{1}$$

for the low defect regime and

$$\frac{I_D}{I_G} = D(\lambda) \cdot {L_D}^2 \tag{2}$$

for the high defect regime. Both formulae were based on a point defect approximation of the Lucchese model [12], where $C'(\lambda)$ = 117 nm^2 for our λ = 532 nm laser, and $D(\lambda)$ was determined by imposing continuity at the border between the two regimes.

We tuned the carrier density of our GFET device and calculated the effect on the mean free path length. The scattering time can be calculated approximately from the conductivity (σ) by

$$\tau = \frac{\hbar\sigma}{e^2 v_F}\sqrt{\frac{\pi}{n}} \tag{3}$$

which can then be transformed into the equation for the mean free path length [52].

$$l = \frac{\hbar\sigma}{e^2}\sqrt{\frac{\pi}{n}} \tag{4}$$

where n is the carrier (doping) density and $l = v_F\tau$, given the Fermi velocity of $v_F \approx 10^6$ m/s [2]. Here, we noted that the mean free path length is strongly related to the doping density, which for our measurements was tuned on the order of 1×10^{15} m^{-2} to 20×10^{15} m^{-2} through back-gate tuning.

We can also extract L_ϕ, L_i and L_* (phase coherence, intervalley and intravalley scattering lengths, respectively) from low-field magneto-transport measurements by first converting resistance to a change in conductivity [14],

$$\Delta\sigma_{xx}(B) = [\sigma_{xx}(B) - \sigma_{xx}(B=0)] - [\sigma_{xx}(B,\ T_h) - \sigma_{xx}(B=0,\ T_h)] \tag{5}$$

with $\sigma_{xx}(B) = \frac{1}{w} \cdot \frac{1}{R_{xx}(B)}$.

In this equation, $\sigma(B, T_h)$ represents the magneto-conductivity at a sufficiently high temperature for the weak localization feature to disappear; T_h is ~60 K as we previously reported [14]. R_{xx} means the two-terminal resistance of the device. The length and width of our graphene sample are represented by l and w respectively. We then fitted this $\Delta\sigma$ to a weak localization theory developed for graphene [15–17]:

$$\begin{gathered}\Delta\sigma_{xx}(B) = \frac{e^2}{\pi h} \cdot \left[F\left(\frac{B}{B_\varphi}\right) - F\left(\frac{B}{B_\varphi + 2B_i}\right) - 2F\left(\frac{B}{B_\varphi + B_i + B_*}\right)\right] \\ \text{with } F(z) = \ln(z) + \Psi\left(\frac{1}{2} + \frac{1}{z}\right) \text{ and } B_{\varphi,i,*} = \left(\frac{h}{8\pi e}\right) L_{\varphi,i,*}^{-2}\end{gathered} \tag{6}$$

where Ψ is the digamma function.

3. Results

We characterize the disorder induced by the electron-beam exposure in Figure 1. First, we performed Raman measurements for an array of graphene samples with different levels of induced disorder by applying irradiation. Figure 1a shows that the D peak intensity increased with the increasing dosage of irradiation, indicating the increasing disorder of the graphene. The I_D/I_G ratio increased from 0.3 at 50 e^-/nm^2 to 4 at 10,000 e^-/nm^2 then decreased to 3.7 at 30,000 e^-/nm^2, indicating a transition into the high-disorder regime. Figure 1b plots the measured resistance for a range of low magnetic fields, where we observed a transition from positive to negative magnetoresistance with the increase of irradiation, with weak localization features appearing at zero fields.

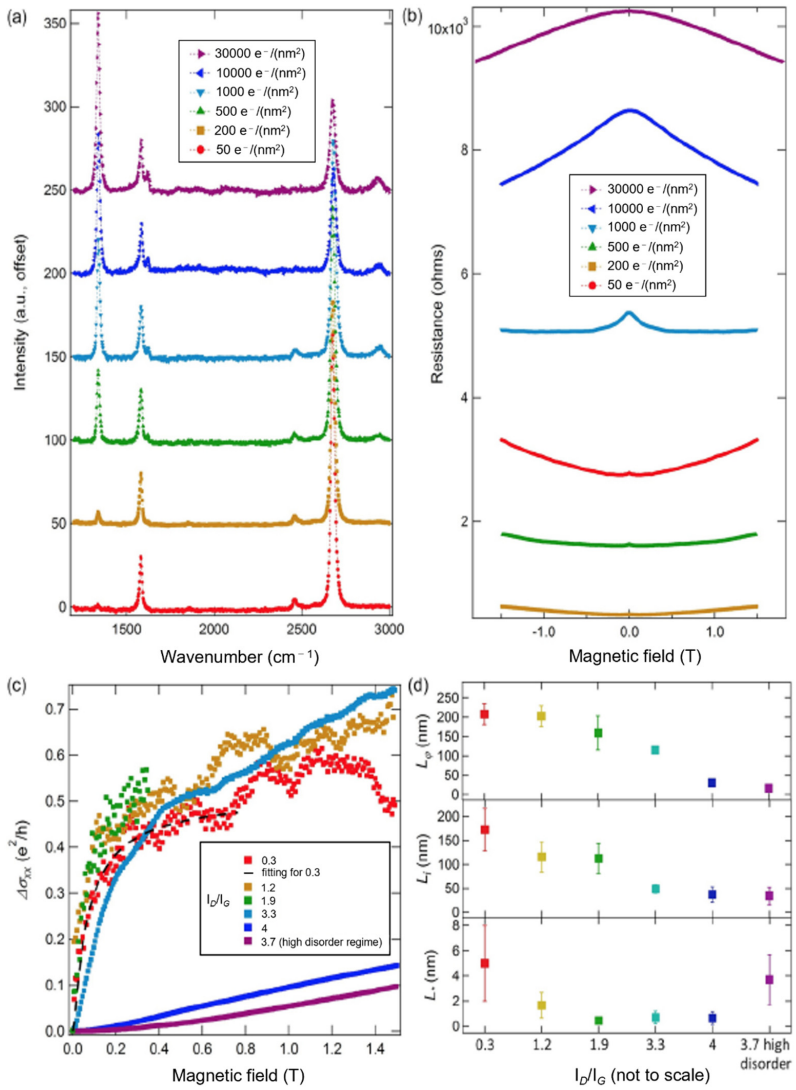

Figure 1. Disorder induced by electron-beam exposure. (**a**) The Raman spectra (excitation wavelength 532 nm) of graphene for a progression of accumulated electron-beam exposures mostly show (except for the last and highest dosage in the high-disorder regime) an increase in the disorder-induced 'D' peak with increased radiation exposure. The spectra are offset vertically for clarity. (**b**) Magnetic field-dependent resistance yields symmetric line shapes that notably develop a central resistance peak associated with weak localization. (**c**) The change in conductivity versus the magnetic field for the same progression of accumulated electron-beam exposures which are denoted by their I_D/I_G ratio derived from part (**a**). (**d**) A comparison that shows the decrease of the scattering length for low-to-high disorder samples, as indicated by the mostly increasing I_D/I_G ratio. The scattering lengths are derived from the conductivity curves in (**c**) using weak localization theory.

This weak localization feature can be seen more clearly in Figure 1c, which shows $\Delta\sigma_{xx}$ versus the magnetic field. The black dotted line in Figure 1c is a representative fitting curve (for the dataset at I_D/I_G = 0.3) using Equation (6) to extract L_ϕ, L_i and L_* from the weak localization model. We performed such fitting for all of the relevant datasets, and the extracted quantities could then be compared to the I_D/I_G ratio from the corresponding Raman measurement. We noted a general trend in Figure 1d of decreasing scattering lengths with an increasing amount of disorder, as indicated by the higher I_D/I_G (up to the high-disorder regime). The value of L_* at the highest disorder (I_D/I_G = 3.7) is larger than the previous value at I_D/I_G = 4, which deviates from the above expectation; the reason is not clear.

In order to add more insights into the observed decrease in scattering length with the increase of irradiation exposure, we also calculated the mean free path, l, for a number of electron-beam exposures using Equation (4) listed above (Figure 2). We found that the trends observed in Figure 1c—decreasing scattering lengths with increasing irradiation dosage—were generally consistent with a trend in l, which decreased with increasing levels of irradiation exposure, from ~95 nm at 500 e^-/nm^2 (shown in orange) to ~5 nm at 30,000 e^-/nm^2 (shown in turquoise) for the lowest tuned doping density, 1×10^{15} m^{-2}. There was an anomalous increase in l between 50 e^-/nm^2 and 500 e^-/nm^2. This may indicate that low-dosage e-beam irradiation could have a possible effect of reducing or removing some of the disorder affecting electronic transport (mean free path l). Furthermore, at relatively low doping, we observed a decrease of the mean free path length, l, when the doping was tuned to higher values.

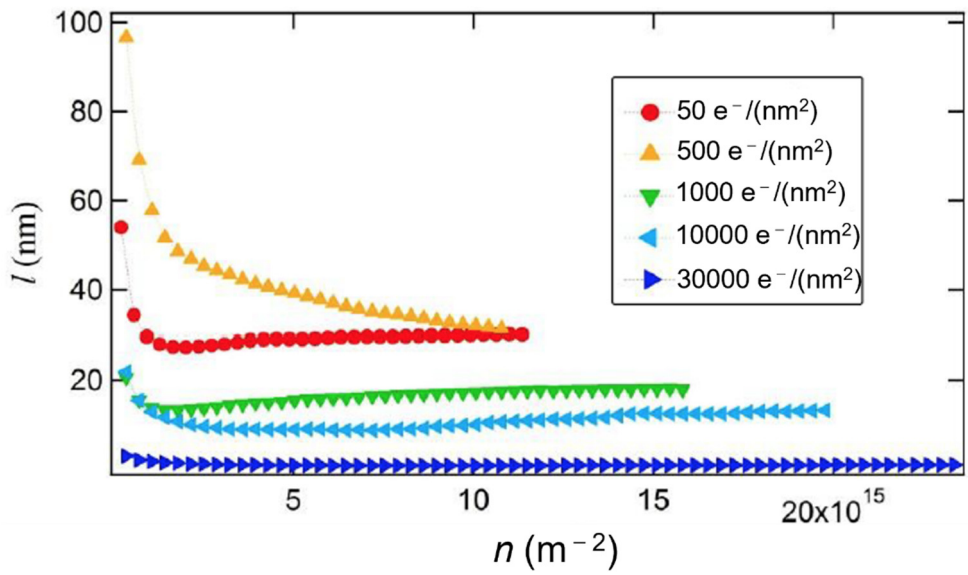

Figure 2. Carrier density dependence of the mean free path. The mean free path, l, versus the carrier density, n, for various levels of e-beam irradiation dosage. When the exposure increases, l tends to decrease because of higher disorder. For each exposure, l increases as the doping density is tuned to the lowest values close to the Dirac point. There is an anomalous increase in l between 50 e^-/nm^2 and 500 e^-/nm^2.

We then used another method to increase disorder in graphene through plasma-etching; we confirm the disorder-induced trends in Figures 1 and 2. An array of plasma-etched samples with different levels of disorder determined by Raman spectroscopy underwent low-field magneto-transport measurements. Figure 3a show $\Delta\sigma_{xx}$ versus the magnetic field for this array of samples identified by their I_D/I_G ratio. The weak localization feature became broader for higher levels of disorder, indicating smaller values of L_ϕ. Figure 3b shows a progression of L_ϕ, L_i and L_* with increasing levels of disorder. Although there were

relatively large uncertainties and error bars in our L_* calculation, L_ϕ and L_i both decreased significantly with the increase of disorder demonstrated by the change of I_D/I_G.

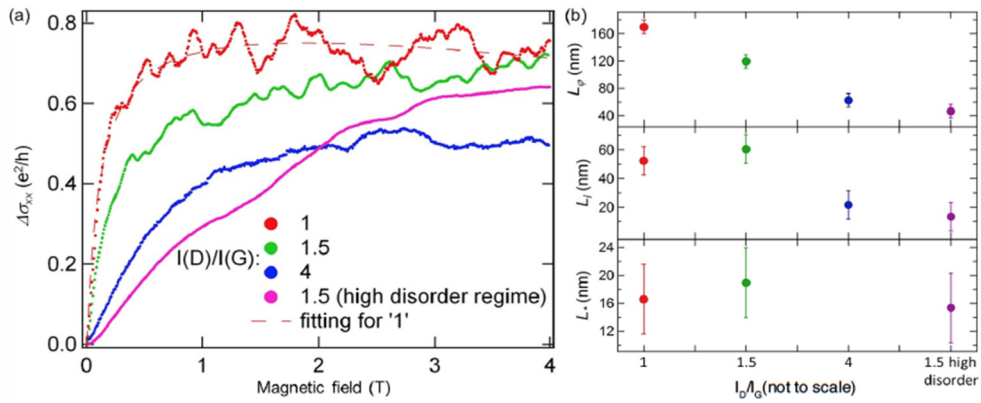

Figure 3. Disorder induced by oxygen plasma. (**a**) Change in conductivity versus the magnetic field for various devices exposed to differing amounts of oxygen plasma. The curves are identified by each device's corresponding I_D/I_G ratio from their Raman spectra. (**b**) A comparison of the weak localization scattering lengths derived from each conductivity curve for the differing I_D/I_G ratios.

4. Discussion

We have ascertained that increasing disorder, either induced by oxygen plasma etching or electron beam irradiation, decreased the defect length (L_D, reflecting the length scale or domain size between defects). This was observed through the progressive growth of the D peak with increasing levels of exposure, characteristic of continuously increased levels of disorder, where we evolve from a low-defect-density regime defined by an increasing I_D/I_G ratio into a high-defect-density regime defined by a decreasing I_D/I_G ratio. When compared to an estimation of the defect length (L_D) derived from the amount of irradiation, the data from the electron-beam exposure could show a somewhat different L_D dependence of I_D/I_G from that for the data from the plasma exposure [14,53]. This indicated that different types of defects could be generated through different processes [12].

This conclusion can be examined further by noting that there was an increased amount of attenuation in the G and 2D peaks at high levels of disorder, which was observed to be much shorter and wider for the oxygen plasma case. The 2D peak became to be almost completely suppressed by higher oxygen plasma exposure, while the 2D peak remained the largest feature with high electron-beam exposures. This indicates that the I_D/I_G progression might be caused by two separate types of defects for each case.

The magneto-transport measurements for each case showed a weak localization feature that became broader when the levels of disorder in the graphene were higher, indicating decreasing phase coherence lengths with the increase of disorder. We also observed a correlation between the decrease in L_D with increasing disorder and the decrease in the characteristic scattering lengths with an increasing disorder caused by both electron-beam irradiation and oxygen plasma etching.

There was an overall trend of L_D and L_ϕ decreasing with the increase of disorder, which was observed separately in previous reports [54–56]. In Figure 4, we plot the L_ϕ, L_i and L_* derived from Equation (6) versus an L_D calculated from the I_D/I_G ratio of the Raman spectrum using Equation (1) (the low-defect-density regime) and Equation (2) (the high-defect-density regime). We saw some linearity in the data, particularly for the plasma-etched samples and at higher disorders levels, estimating an L_ϕ around 15 times larger than L_D and an L_i about five times larger than L_D. However, at lower levels of disorder, there was a nonlinear relationship between L_D and L_ϕ. This may be due to how L_D here characterizes relatively isolated and dilute defects created by irradiation and not 1D-like line defects separating crystallites, which could impact intravalley and intervalley scattering more. For example, the change in L_D could reflect the more-changing number and distribution

of point defects, and not so much the introduction of periodic line defects which majorly impacted scattering in [57].

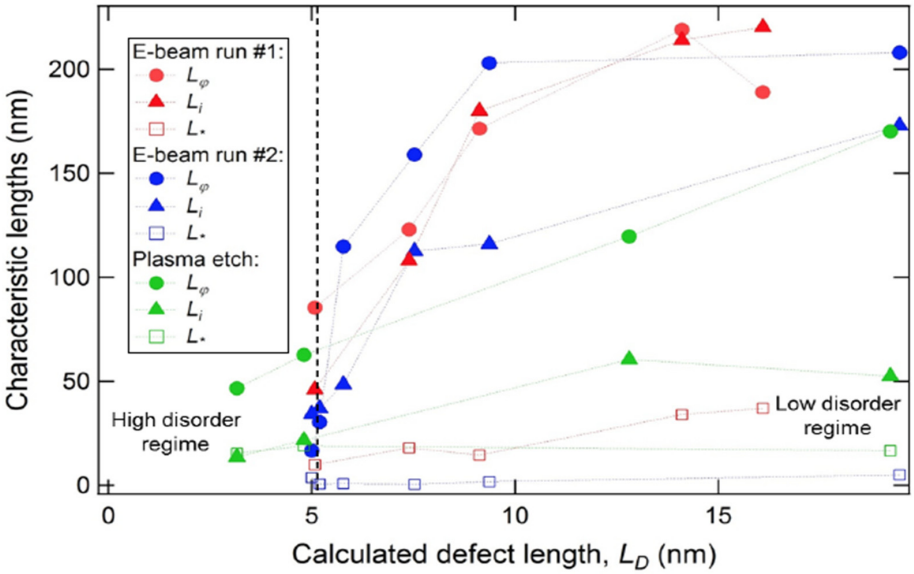

Figure 4. Correlation between the transport (weak location) extracted lengths and Raman extracted lengths, and a comparison between plasma etching and electron-beam exposure cases. Weak localization scattering lengths derived from Equation (6) versus the Raman defect length derived from Equations 1 and 2 for two separate sets of e-beam irradiation data and a set of plasma etching data. The vertical dashed line represents the transition from the low-disorder regime (right) to the high-disorder regime (left).

We have demonstrated, in this study, how Raman spectra and magneto-transport are affected by disorder and carrier density. It is worth investigating further the discrepancies between our electron-beam and oxygen plasma data in order to better determine the nature of the defects in each case, and to determine why the shape of the high-disorder spectra look different in each case, specifically the shapes of the G and 2D peaks. More research is also needed in order to figure out how the Raman spectra of graphene—and specifically the disorder D peak—are affected by other parameters such as temperature or strain. In summary, the findings in this study are valuable for a better understanding of the relationship between the disorder density of graphene and transport parameters like phase coherence and scattering lengths. Furthermore, our analysis of the disorder caused by oxygen plasma and electron-beam irradiation enhances our knowledge of charge carrier behavior within the context of weak localization.

Author Contributions: Conceptualization, I.C. and Y.P.C.; methodology, I.C.; formal analysis, I.C. and J.F.R.; investigation, I.C., M.A.S. and H.C.; data curation, Y.Q.; writing—original draft preparation, I.C., J.F.R. and H.C.; writing—review and editing, Y.Q., M.A.S. and Y.P.C.; supervision, Y.P.C. and Y.Q.; project administration, Y.P.C. and Y.Q.; funding acquisition, Y.P.C. and Y.Q. All authors have read and agreed to the published version of the manuscript.

Funding: Various aspects and stages of this research were funded by the National Science Foundation (NSF), grant numbers 0847638, 0833689, 1711332, and Macau Science and Technology Development Fund, grant numbers 0106/2020/A3 and 0031/2021/ITP.

Institutional Review Board Statement: Not applicable.

Informed Consent Statement: Not applicable.

Data Availability Statement: Not applicable.

Conflicts of Interest: The authors declare no conflict of interest.

References

1. Raza, H. *Graphene Nanoelectronics: Metrology, Synthesis, Properties and Applications*; Springer Science & Business: Berlin, Germany, 2012.
2. Geim, A.K.; Novoselov, K.S. The rise of graphene. *Nat. Mater.* **2007**, *6*, 183–191. [CrossRef] [PubMed]
3. Saito, R.; Hofmann, M.; Dresselhaus, G.; Jorio, A.; Dresselhaus, M.S. Raman spectroscopy of graphene and carbon nanotubes. *Adv. Phys.* **2011**, *60*, 413–550. [CrossRef]
4. Ferrari, A.C.; Basko, D.M. Raman spectroscopy as a versatile tool for studying the properties of graphene. *Nat. Nanotechnol.* **2013**, *8*, 235–246. [CrossRef] [PubMed]
5. Jang, J.I. *New Developments in Photon and Materials Research*; Nova Publishers: New York, NY, USA, 2014.
6. Ferrari, A.C.; Meyer, J.C.; Scardaci, V.; Casiraghi, C.; Lazzeri, M.; Mauri, F.; Piscanec, S.; Jiang, D.; Novoselov, K.S.; Roth, S.; et al. Raman Spectrum of Graphene and Graphene Layers. *Phys. Rev. Lett.* **2006**, *97*, 187401. [CrossRef] [PubMed]
7. Ferrari, A.C. Raman spectroscopy of graphene and graphite: Disorder, electron–phonon coupling, doping and nonadiabatic effects. *Solid State Commun.* **2007**, *143*, 47–57. [CrossRef]
8. Tuinstra, F.; Koenig, J.L. Raman Spectrum of Graphite. *J. Chem. Phys.* **1970**, *53*, 1126–1130. [CrossRef]
9. Teweldebrhan, D.; Balandin, A.A. Response to 'Comment on "Modification of graphene properties due to electron-beam irradiation"'. *Appl. Phys. Lett.* **2009**, *95*, 246102. [CrossRef]
10. Martins Ferreira, E.H.; Moutinho, M.V.O.; Stavale, F.; Lucchese, M.M.; Capaz, R.B.; Achete, C.A.; Jorio, A. Evolution of the Raman spectra from single-, few-, and many-layer graphene with increasing disorder. *Phys. Rev. B Condens. Matter Mater. Phys.* **2010**, *82*, 125429. [CrossRef]
11. Childres, I.; Jauregui, L.A.; Foxe, M.; Tian, J.; Jalilian, R.; Jovanovic, I.; Chen, Y.P. Effect of electron-beam irradiation on graphene field effect devices. *Appl. Phys. Lett.* **2010**, *97*, 173109. [CrossRef]
12. Lucchese, M.M.; Stavale, F.; Ferreira, E.M.; Vilani, C.; Moutinho, M.V.D.O.; Capaz, R.B.; Achete, C.A.; Jorio, A. Quantifying ion-induced defects and Raman relaxation length in graphene. *Carbon* **2010**, *48*, 1592–1597. [CrossRef]
13. Cançado, L.G.; Takai, K.; Enoki, T.; Endo, M.; Kim, Y.A.; Mizusaki, H.; Jorio, A.; Coelho, L.N.; Magalhães-Paniago, R.; Pimenta, M.A. General equation for the determination of the crystallite size La of nanographite by Raman spectroscopy. *Appl. Phys. Lett.* **2006**, *88*, 163106. [CrossRef]
14. Childres, I.; Jauregui, L.A.; Tian, J.; Chen, Y.P. Effect of oxygen plasma etching on graphene studied using Raman spectroscopy and electronic transport measurements. *New J. Phys.* **2011**, *13*, 025008. [CrossRef]
15. McCann, E.; Kechedzhi, K.; Fal'ko, V.I.; Suzuura, H.; Ando, T.; Altshuler, B.L. Weak-localization magnetoresistance and valley symmetry in graphene. *Phys. Rev. Lett.* **2006**, *97*, 146805. [CrossRef] [PubMed]
16. Mucciolo, E.R.; Lewenkopf, C.H. Disorder and electronic transport in graphene. *J. Phys. Condens. Matter* **2010**, *22*, 273201. [CrossRef] [PubMed]
17. Tikhonenko, F.V.; Horsell, D.W.; Gorbachev, R.V.; Savchenko, A.K. Weak Localization in graphene flakes. *Phys. Rev. Lett.* **2008**, *100*, 056802. [CrossRef]
18. Morsin, M.; Isaak, S.; Morsin, M.; Yusof, Y. Controlled defect on multilayer graphene surface by oxygen plasma. *AIP Conf. Proc.* **2017**, *1788*, 030117.
19. Morsin, M.; Isaak, S.; Morsin, M.; Yusof, Y. Characterization of defect induced multilayer graphene. *Int. J. Electr. Comput. Eng.* **2017**, *7*, 1452–1458. [CrossRef]
20. Li, H.; Singh, A.; Bayram, F.; Childress, A.S.; Rao, A.M.; Koley, G. Impact of oxygen plasma treatment on carrier transport and molecular adsorption in graphene. *Nanoscale* **2019**, *11*, 11145–11151. [CrossRef]
21. Xie, G.B.; Yang, R.; Chen, P.; Zhang, J.; Tian, X.; Wu, S.; Zhao, J.; Cheng, M.; Yang, W.; Wang, D.; et al. A general route towards defect and pore engineering in graphene. *Small* **2014**, *10*, 2280–2284. [CrossRef]
22. Cançado, L.G.; Jorio, A.; Ferreira, E.M.; Stavale, F.; Achete, C.A.; Capaz, R.B.; Moutinho, M.V.D.O.; Lombardo, A.; Kulmala, T.S.; Ferrari, A.C. Quantifying defects in graphene via Raman spectroscopy at different excitation energies. *Nano Lett.* **2011**, *11*, 3190–3196. [CrossRef]
23. Zhou, Y.B.; Liao, Z.M.; Wang, Y.F.; Duesberg, G.S.; Xu, J.; Fu, Q.; Wu, X.S.; Yu, D.P. Ion irradiation induced structural and electrical transition in graphene. *J. Chem. Phys.* **2010**, *133*, 234703. [CrossRef] [PubMed]
24. Zhong, J.H.; Zhang, J.; Jin, X.; Liu, J.Y.; Li, Q.; Li, M.H.; Cai, W.; Wu, D.Y.; Zhan, D.; Ren, B. Quantitative correlation between defect density and heterogeneous electron transfer rate of single layer graphene. *J. Am. Chem. Soc.* **2014**, *136*, 16609–16617. [CrossRef]
25. Zafar, Z.; Ni, Z.H.; Wu, X.; Shi, Z.X.; Nan, H.Y.; Bai, J.; Sun, L.T. Evolution of Raman spectra in nitrogen doped graphene. *Carbon* **2013**, *61*, 57–62. [CrossRef]
26. Sun, Y.B.; Zhang, M.; Dong, L.; Wang, G.; Xie, X.; Wang, X.; Hu, T.; Di, Z. Weak localization behavior observed in graphene grown on germanium substrate. *AIP Adv.* **2018**, *8*, 045214. [CrossRef]
27. Pezzini, S.; Cobaleda, C.; Diez, E.; Bellani, V. Disorder and de-coherence in graphene probed by low-temperature magneto-transport: Weak localization and weak antilocalization. *J. Phys. Conf. Ser.* **2013**, *456*, 012032. [CrossRef]
28. Wang, W.R.; Chen, L.; Wang, Z.; Wang, Y.; Li, T.; Wang, Y. Weak localization in few-layer graphene grown on copper foils by chemical vapor deposition. *Carbon* **2012**, *50*, 5242–5246. [CrossRef]
29. Gonnelli, R.S.; Piatti, E.; Sola, A.; Tortello, M.; Dolcini, F.; Galasso, S.; Nair, J.R.; Gerbaldi, C.; Cappelluti, E.; Bruna, M.; et al. Weak localization in electric-double-layer gated few-layer graphene. *2D Mater.* **2017**, *4*, 035006. [CrossRef]

30. Zion, E.; Haran, A.; Butenko, A.V.; Wolfson, L.; Kaganovskii, Y.; Havdala, T.; Sharoni, A.; Naveh, D.; Richter, V.; Kaveh, M.; et al. Localization of charge carriers in monolayer graphene gradually disordered by ion irradiation. *Graphene* **2015**, *4*, 45–53. [CrossRef]
31. Banhart, F.; Kotakoski, J.; Krasheninnikov, A.V. Structural defects in graphene. *ACS Nano* **2011**, *5*, 26–41. [CrossRef]
32. Eckmann, A.; Felten, A.; Mishchenko, A.; Britnell, L.; Krupke, R.; Novoselov, K.S.; Casiraghi, C. Probing the nature of defects in graphene by Raman spectroscopy. *Nano Lett.* **2012**, *12*, 3925–3930. [CrossRef]
33. Liu, L.; Qing, M.; Wang, Y.; Chen, S. Defects in graphene: Generation, healing, and their effects on the properties of graphene: A review. *J. Mater. Sci. Technol.* **2015**, *31*, 599–606. [CrossRef]
34. Gawlik, G.; Ciepielewski, P.; Baranowski, J.M. Study of implantation defects in CVD graphene by optical and electrical methods. *Appl. Sci.* **2019**, *9*, 544. [CrossRef]
35. Vinchon, P.; Glad, X.; Robert Bigras, G.; Martel, R.; Stafford, L. Preferential self-healing at grain boundaries in plasma-treated graphene. *Nat. Mater.* **2021**, *20*, 49–54. [CrossRef]
36. Baker, A.M.R.; Alexander-Webber, J.A.; Altebaeumer, T.; Janssen, T.J.B.M.; Tzalenchuk, A.; Lara-Avila, S.; Kubatkin, S.; Yakimova, R.; Lin, C.T.; Li, L.J.; et al. Weak localization scattering lengths in epitaxial, and CVD graphene. *Phys. Rev. B* **2012**, *86*, 235441. [CrossRef]
37. Hilke, M.; Massicotte, M.; Whiteway, E.; Yu, V. Weak localization in graphene: Theory, simulations, and experiments. *Sci. World J.* **2014**, *2014*, 737296. [CrossRef]
38. Drabińska, A.; Kaźmierczak, P.; Bożek, R.; Karpierz, E.; Wołoś, A.; Wysmołek, A.; Kamińska, M.; Pasternak, I.; Krajewska, A.; Strupiński, W. Electron scattering in graphene with adsorbed NaCl nanoparticles. *J. Appl. Phys.* **2015**, *117*, 014308. [CrossRef]
39. Ilić, S.; Meyer, J.S.; Houzet, M. Weak localization in transition metal dichalcogenide monolayers and their heterostructures with graphene. *Phys. Rev. B* **2019**, *99*, 205407. [CrossRef]
40. Wang, X.; Wang, H.; Chen, L.; He, L.; Chen, C.; Jiang, C.; Qiu, Z.; Wang, H.; Xie, X. Weak localization in graphene sandwiched by aligned h-BN flakes. *Nanotechnology* **2020**, *31*, 215712. [CrossRef]
41. Abbas, M.S.; Srivastava, P.K.; Hassan, Y.; Lee, C. Asymmetric carrier transport and weak localization in few layer graphene grown directly on a dielectric substrate. *Phys. Chem. Chem. Phys.* **2021**, *23*, 25284–25290. [CrossRef] [PubMed]
42. Kim, M.; Safron, N.S.; Han, E.; Arnold, M.S.; Gopalan, P. Electronic transport and Raman scattering in size-controlled nanoperforated graphene. *ACS Nano* **2012**, *6*, 9846–9854. [CrossRef]
43. Oberhuber, F.; Blien, S.; Heydrich, S.; Yaghobian, F.; Korn, T.; Schüller, C.; Strunk, C.; Weiss, D.; Eroms, J. Weak localization and Raman study of anisotropically etched graphene antidots. *Appl. Phys. Lett.* **2013**, *103*, 143111. [CrossRef]
44. Wang, P.H.; Shih, F.Y.; Chen, S.Y.; Hernandez, A.B.; Ho, P.H.; Chang, L.Y.; Chen, C.H.; Chiu, H.C.; Chen, C.W.; Wang, W.H. Demonstration of distinct semiconducting transport characteristics of monolayer graphene functionalized via plasma activation of substrate surfaces. *Carbon* **2015**, *93*, 353–360. [CrossRef]
45. Kierdaszuk, J.; Kaźmierczak, P.; Drabińska, A.; Korona, K.; Wołoś, A.; Kamińska, M.; Wysmołek, A.; Pasternak, I.; Krajewska, A.; Pakuła, K. Enhanced Raman scattering and weak localization in graphene deposited on GaN nanowires. *Phys. Rev. B.* **2015**, *92*, 195403. [CrossRef]
46. Coleman, C.; McIntosh, R.; Bhattacharyya, S. Controlling the activation energy of graphene-like thin films through disorder induced localization. *J. Appl. Phys.* **2013**, *114*, 043716. [CrossRef]
47. Fujimoto, A.; Perini, C.J.; Terasawa, D.; Fukuda, A.; Harada, Y.; Sasa, S.; Yano, M.; Vogel, E.M. Disorder and weak localization near charge neutral point in Ti-cleaned single-layer graphene. *Phys. Status Solidi B* **2019**, *256*, 1800541. [CrossRef]
48. Blake, P.; Hill, E.W.; Castro Neto, A.H.; Novoselov, K.S.; Jiang, D.; Yang, R.; Booth, T.J.; Geim, A.K. Making graphene visible. *Appl. Phys. Lett.* **2007**, *91*, 063124. [CrossRef]
49. Tao, L.; Qiu, C.; Yu, F.; Yang, H.; Chen, M.; Wang, G.; Sun, L. Modification on single-layer graphene induced by low-energy electron-beam irradiation. *J. Phys. Chem. C* **2013**, *117*, 10079–10085. [CrossRef]
50. Teweldebrhan, D.B. 2D Dirac Materials: From Graphene to Topological Insulators. Ph.D. Thesis, UC Riverside, Riverside, CA, USA, 2011.
51. Kim, D.C.; Jeon, D.Y.; Chung, H.J.; Woo, Y.; Shin, J.K.; Seo, S. The structural and electrical evolution of graphene by oxygen plasma-induced disorder. *Nanotechnology* **2009**, *20*, 375703. [CrossRef]
52. Tan, Y.W.; Zhang, Y.; Bolotin, K.; Zhao, Y.; Adam, S.; Hwang, E.H.; Sarma, S.D.; Stormer, H.L.; Kim, P. Measurement of scattering rate and minimum conductivity in graphene. *Phys. Rev. Lett.* **2007**, *99*, 246803. [CrossRef] [PubMed]
53. Childres, I.; Jauregui, L.A.; Park, W.; Cao, H.; Chen, Y.P. Raman spectroscopy of graphene and related materials. In *New Developments in Photon in and Materials Research*; Nova Science Publishers: New York, NY, USA, 2013; Chapter 19; pp. 1–20.
54. Qin, Y.; Han, J.; Guo, G.; Du, Y.; Li, Z.; Song, Y.; Pi, L.; Wang, X.; Wan, X.; Han, M.; et al. Enhanced quantum coherence in graphene caused by Pd cluster deposition. *Appl. Phys. Lett.* **2015**, *106*, 023108. [CrossRef]
55. Kim, N.-H.; Shin, Y.S.; Park, S.; Kim, H.S.; Lee, J.S.; Ahn, C.W.; Lee, J.O.; Doh, Y.J. Quantum interference effects in chemical vapor deposited graphene. *Curr. Appl. Phys.* **2016**, *16*, 31–36. [CrossRef]
56. Yu, C.; Li, J.; Gao, K.; Lin, T.; Liu, Q.; Dun, S.; He, Z.; Cai, S.; Feng, Z. Observation of quantum hall effect and weak localization in p-type bilayer epitaxial graphene on SiC(0001). *Solid State Commun.* **2013**, *175-176*, 119–122. [CrossRef]
57. Rodrigues, J.N.B. Intervalley scattering of graphene massless Dirac fermions at 3-periodic grain boundaries. *Phys. Rev. B* **2016**, *94*, 134201. [CrossRef]